Frustrated spin correlations in diluted spin ice $Ho_{2-x}La_xTi_2O_7$

G Ehlers[1]**, E Mamontov**[1]**, M Zamponi**[1,2]**, A Faraone**[3,4]**, Y Qiu**[3,4]**,
A L Cornelius**[5]**, C H Booth**[6]**, K C Kam**[7]**, R Le Toquin**[7]**,
A K Cheetham**[7] **and J S Gardner**[4,8]

[1] Spallation Neutron Source, Oak Ridge National Laboratory, Building 8600, Oak Ridge, TN 37831-6475, USA

[2] Jülich Center for Neutron Science, FZ Jülich, 52425 Jülich, Germany

[3] Department of Materials Science and Engineering, University of Maryland, College Park, MD 20742-2115, USA

[4] NIST Center for Neutron Research, NIST, Gaithersburg, MD 20899-6102, USA

[5] Physics Department, University of Nevada Las Vegas, Las Vegas, NV 89154-4002, USA

[6] Chemical Sciences Division, Lawrence Berkeley National Laboratory, Berkeley, CA 94720, USA

[7] Materials Research Laboratory, University of California, Santa Barbara, CA 93106, USA

[8] Indiana University, 2401 Milo B Sampson Lane, Bloomington, IN 47408, USA

E-mail: ehlersg@ornl.gov

Abstract
We have studied the evolution of the structural properties as well as the static and dynamic spin correlations of spin ice $Ho_2Ti_2O_7$, where Ho was partially replaced by non-magnetic La. The crystal structure of diluted samples $Ho_{2-x}La_xTi_2O_7$ was characterized by x-ray and neutron diffraction and by Ho L_{III}-edge and Ti K-edge extended x-ray absorption fine structure (EXAFS) measurements. It is found that the pyrochlore structure remains intact until about $x = 0.3$, but a systematic increase in local disorder with increasing La concentration is observed in the EXAFS data, especially from the Ti K edge.

Quasi-elastic neutron scattering and ac susceptibility measurements show that, in $x \leqslant 0.4$ samples at temperatures above macroscopic freezing, the spin–spin correlations are short ranged and dynamic in nature. The main difference with pure spin ice in the dynamics is the appearance of a second, faster, relaxation process.

(Some figures in this article are in colour only in the electronic version)

1. Introduction

Over the last decade, the spin ices $Dy_2Ti_2O_7$ (DTO) and $Ho_2Ti_2O_7$ (HTO) have been established as topical materials in the context of frustrated magnetism [1, 2]. These systems provide a magnetic analogue to water ice with its residual entropy at low temperature, which is caused by a macroscopic degeneracy of ground states and a particular freezing process [3].

The static spin correlations in the frozen ice state below $T \sim 1$ K have been characterized on a microscopic level by neutron diffraction [4] and are reasonably well understood in terms of the dipolar spin ice model [5]. At $T = 50$ mK, in zero applied field, neutron diffraction has shown static disorder with a correlation length on the order of one lattice spacing, and a local spin arrangement in states obeying the '2 in–2 out' ice rules. Under the same conditions, muon spin relaxation (μSR) has found evidence for residual spin dynamics in both HTO and DTO, a discrepancy which remains to be resolved [6, 7].

The dynamics of spin ice materials at higher temperatures was first studied by ac susceptibility measurements, which confirmed the macroscopic spin freezing through a vanishing real part of the susceptibility $\chi'(\omega)$ and a corresponding maximum in the imaginary part $\chi''(\omega)$ around $T \sim 1$ K [8, 9]. These measurements also revealed a second peak in $\chi''(\omega)$ in DTO at $T \sim 15$ K (i.e. well within the paramagnetic
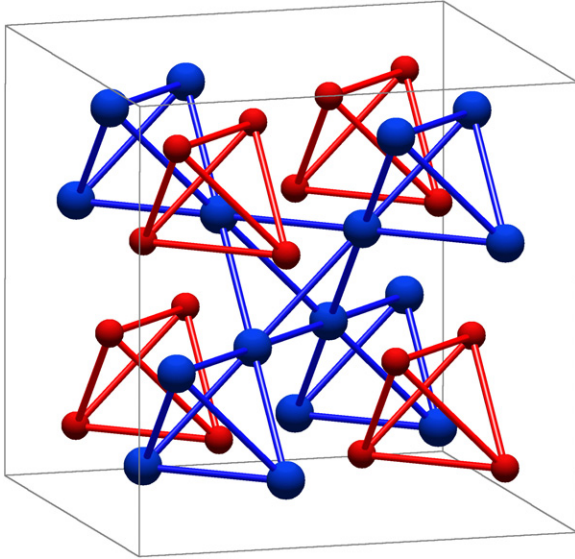
Figure 1. A unit cell of the cubic pyrochlore structure showing the rare-earth (large blue spheres) and titanium (small (red) spheres) sublattices.

phase) that was initially not seen in HTO. In studies on diluted systems $Dy_{2-x}Y_xTi_2O_7$, this peak was found to vanish with Y doping [10, 11] and then to re-emerge in very dilute systems [12]. Subsequently, it was shown by neutron scattering that the peak is intrinsically also present in HTO [13]. All dynamical studies agreed in finding that the distribution of spin relaxation times in these systems is very narrow, with little effect of doping, and that no long-range order was induced by doping down to 100 mK [14, 15].

In this paper, we are interested in studying the evolution of the static and dynamic spin correlations of HTO when Ho is partially replaced by La. The main difference with an earlier study of the $(Ho-Y)_2Ti_2O_7$ solid solution [15] is that the larger La^{3+} ion is expected to create significantly more strain and chemical pressure in the lattice than the Y^{3+} ion. Therefore a major part of this paper is devoted to a characterization of the structural properties of the samples by means of different scattering techniques.

The crystalline symmetry of the pyrochlore phase $A_2B_2O_7$ depends mostly on the cationic ratio r_A/r_B. It has been shown that if this ratio is in the range $1.46 \leqslant r_A/r_B \leqslant 1.78$, the compound may adopt the cubic pyrochlore structure (space group $Fd\bar{3}m$) [16]. This structure is depicted in figure 1. While HTO is cubic with $r_A/r_B = 1.68$, pure $La_2Ti_2O_7$ (LTO) with $r_A/r_B = 1.92$ is known to crystallize in a monoclinic layered structure related to the perovskites (space group $P2_1$) [17].

2. Sample preparation and experimental techniques

Solid-solution samples with composition $Ho_{2-x}La_xTi_2O_7$, $0 \leqslant x \leqslant 1.8$, were prepared by mixing Ho_2O_3, La_2O_3, and TiO_2 powders (purity 99.9%) in stoichiometric proportions. Each sample was heated up to 1400 °C in air at 5 °C min^{-1} for a period of four days with intermediate grindings. Powder x-ray

diffraction data were analysed by means of Rietveld refinement using the *Fullprof* software [18].

Samples with $x = 0$, 0.1, 0.4 and 1.7 were prepared for extended x-ray absorption fine structure (EXAFS) measurements by further grinding them in a mortar and pestle, passing them through a 20 μm sieve, brushing the resulting powder onto adhesive tape, and then stacking the tape to achieve a sample thickness t such that the change in the absorption μ at the edge corresponded to $\Delta\mu t \approx 1$. The samples were placed in a LHe-flow cryostat, and transmission data were recorded at the Ho L_{III} and Ti K edges at $T = 30$ K. Data were collected on beam line 10-2 at the Stanford Synchrotron Radiation Laboratory, using a half-tuned Si(220) double monochromator. The data were analysed using standard procedures [19]. In particular, the embedded atom absorption μ_0 was determined using a cubic spline with 5 knots over the data range, which was typically about 1 keV above the absorption threshold, E_0, as determined by the position of the half-height of the absorption change at the edge. The data were fitted in r-space using the RSXAP package [20] with theoretical scattering functions generated by FEFF7 [21].

Samples were then characterized by ac susceptibility measurements, in an external field up to 1 T, using commercially available fully calibrated magnetic measurement equipment. These measurements provide access to slow spin dynamics complementary to neutron scattering techniques.

Neutron diffraction was measured at room temperature at the BT-1 powder diffractometer at the NIST Center for Neutron Research in Gaithersburg, MD, USA. A wavelength of $\lambda = 1.54$ Å was chosen from a Cu-(311) Bragg reflection. Quasi-elastic neutron time-of-flight (TOF) measurements were performed at the Disk Chopper Spectrometer (DCS) [22] at the NIST Center for Neutron Research (NIST NCNR) with an incident wavelength of 5.0 Å, giving an energy resolution of ∼110 μeV full width at half-maximum (FWHM). The scattering patterns were appropriately corrected for sample transmission, background and detector efficiency using measurements of an empty container and a vanadium reference sample.

Neutron backscattering (BS) measurements were made at the new beam line 2 instrument at the Spallation Neutron Source (SNS) at Oak Ridge National Laboratory (ORNL) [23]. In backscattering, one uses a polychromatic incident neutron beam and Si(111) analyser crystals to select the final energy of 2082 μeV ($\lambda = 6.267$ Å) for scattered neutrons. At the elastic line the energy resolution was ∼3 μeV. At the time of the experiments, SNS was running at 30 Hz, making a dynamic range of more than ±400 μeV accessible. In these experiments, a vanadium reference sample was also measured. The neutron spin echo (NSE) [24] experiments were performed at the NSE spectrometer at the NIST NCNR using a neutron wavelength of $\lambda = 6$ Å (bandwidth of 20%). This setting gives a Fourier time range of 40 ps $\leqslant t \leqslant 10$ ns, over which correlations can be studied. Two values for the momentum transfer Q were chosen: $Q = 0.4$ and 0.7 Å^{-1}. Instrumental resolution was measured with a $Ho_{0.7}Y_{1.3}Ti_2O_7$ sample, which is known to be static on the probed timescale at a temperature around or below $T \sim 5$ K [15].
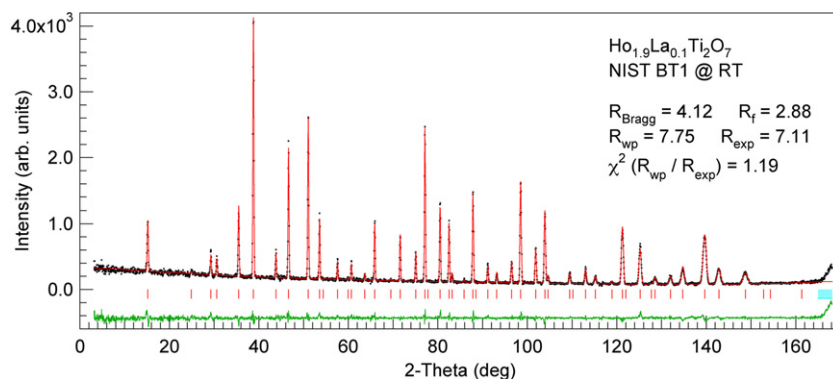
Figure 2. Neutron powder diffraction pattern and Rietveld refinement of the $x = 0.1$ sample measured at room temperature. Shown are the observed counts, the calculated profile, and the difference. Bragg positions are marked by vertical ticks.

Table 1. Refinement results from neutron diffraction for the $Ho_{1.9}La_{0.1}Ti_2O_7$ sample. Isotropic displacement factors were refined only for the oxygen sites.

| Compound $Ho_{1.9}La_{0.1}Ti_2O_7$ Symmetry $Fd\bar{3}m$ $a = 10.1182(1)$ Å					
Position	Atom	Occ.	Ideal occ.	x, y, z	β_{iso}
16d	Ho	0.0792	0.0792	$\frac{1}{2}, \frac{1}{2}, \frac{1}{2}$	0.3
16d	La	0.0041	0.0041	$\frac{1}{2}, \frac{1}{2}, \frac{1}{2}$	0.3
16c	Ti	0.0833	0.0833	0, 0, 0	0.3
48f	O	0.255(1)	0.2500	0.3284(1), $\frac{1}{8}, \frac{1}{8}$	0.53(1)
8b	O	0.043(0)	0.0417	$\frac{3}{8}, \frac{3}{8}, \frac{3}{8}$	0.53(1)

3. Results

3.1. X-ray and neutron diffraction

A neutron diffraction pattern of the $x = 0.1$ sample is shown in figure 2. The refined model parameters are summarized in table 1.

All structural parameters resulting from the refinement are very close to the ideal pyrochlore structure (space group $Fd\bar{3}m$). The $x = 0.2$ compound is also purely monophasic pyrochlore. Due to the larger ionic radius of La^{3+}, the cell parameter of the cubic cell increases from 10.1000 Å for pure HTO to 10.1419(5) Å for $x = 0.2$. At further increasing La concentration, extra peaks corresponding to an LTO phase are observed in the x-ray powder diffraction pattern. The samples essentially split into two co-existing phases, which are identified as La-doped HTO and Ho-doped LTO, respectively. The amount of LTO phase increases until x reaches a value of about 1.7, where only the LTO phase is present. Figure 3 shows that the sample separation into two phases depends linearly on the doping parameter x. In particular, it is mentioned here that the $x = 0.4$ sample had a 10% content of the LTO phase.

The cell parameter of the Ho-rich (HTO) phase is nearly constant at 10.1419 Å throughout the bi-phasic region, which suggests that some amount of La goes into the Ho site until a certain level of strain is reached, which the cubic phase cannot accommodate any more. These results are thus quite similar to the $Y_{2-x}La_xTi_2O_7$ series [25]. For completeness,
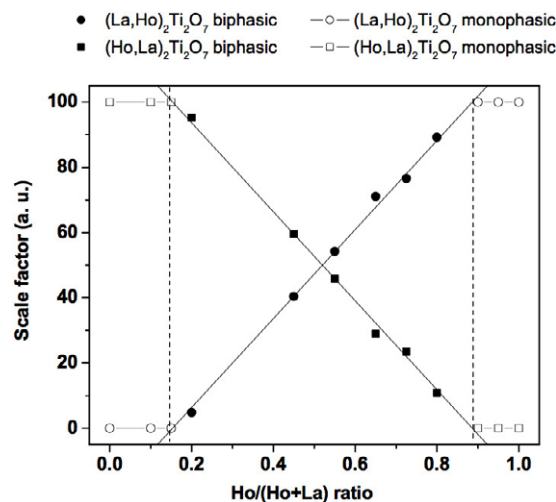

Figure 3. Evolution of the refined values of the scale factors of the pure HTO and LTO phases upon substitution, from pure LTO phase (left) to pure HTO phase (right). The sum of the two phases has been fixed to 100.

it is mentioned that monoclinic LTO phase had refined cell parameter values of $a = 7.7657(12)$ Å, $b = 5.5136(9)$ Å, $c = 13.0013(24)$ Å and $\beta = 98.58(58)°$ which were also nearly constant throughout the bi-phasic region. From the diffraction results it was concluded that a study of the magnetic properties should be limited to the composition range $x \leqslant 0.4$.

3.2. EXAFS

The pyrochlore structure possesses a fairly straightforward local structure around the Ho and Ti sites, except that the six nearest-neighbour Ho–Ti (Ti–Ho) pairs are directly overlapping with the six nearest-neighbour Ho–Ho (Ti–Ti) pairs near 3.58 Å. The additional presence of La in the structure further complicates the fitting of this peak, so the same procedure was employed as in previous EXAFS studies of pyrochlores [15, 26, 27], namely, for a given edge (e.g. Ho L_{III}), the overlapping pairs near 3.58 Å (Ho–Ti, Ho–Ho and Ho–La) were constrained to the same pair separation distance, and the pair-distribution variances (σ^2) were
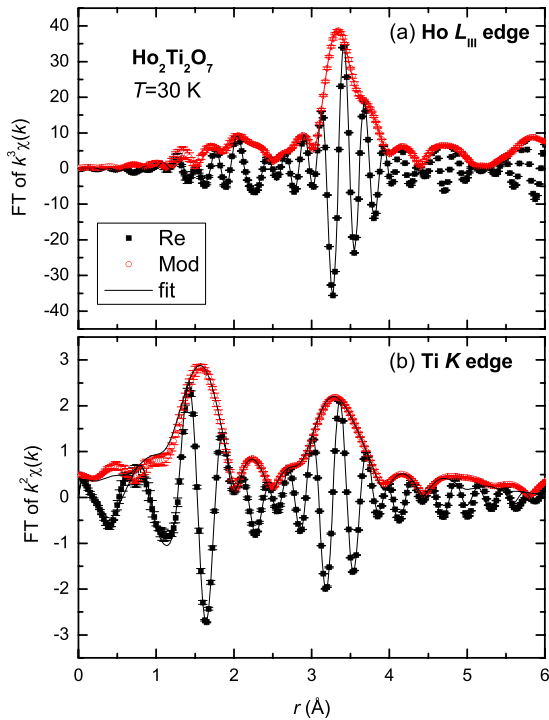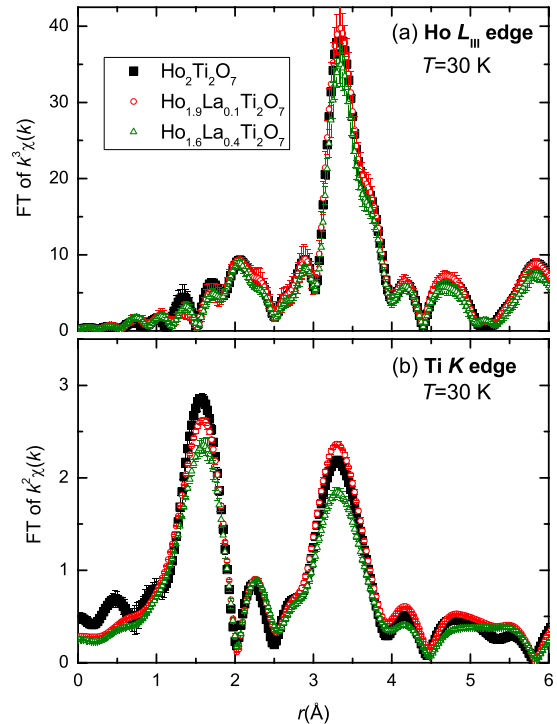
Figure 4. (a) FT of the $k^3\chi(k)$ EXAFS data from the Ho L_{III} edge and (b) FT of the $k^2\chi(k)$ of $T = 30$ K data from the Ti K edge of pure $Ho_2Ti_2O_7$ are shown together with fits. Transform ranges are between 2.5–14.4 and 3.5–11.4 Å^{-1} respectively, all Gaussian broadened by 0.3 Å^{-1}. Error bars are based on the reproducibility over multiple scans.

constrained to the ratio of the reduced masses of the particular scatter pairs.

An additional constraint occurs because of the proximity of the La L_{III} edge to the Ti K edge. The Ti K edge (about 4965 eV) data range was limited to about 11.4 Å^{-1} in samples with $x \neq 0$ by the presence of the La L_{III} edge at about 5483 eV. For such a short k-range, the correlation between the overall amplitude factor, S_0^2, and the σ^2 parameters in the fit is expected to be very strong. S_0^2 was therefore obtained from fits to the $x = 0$ data using a wide (2.5–16 Å^{-1}) transform range, and then held fixed to this value for fits to the data from the other samples. A similar procedure was used for the Ho edge data, although only one transform range was required. It is noted that the overlap between the Ti and La edges even more severely limits the usability of the La L_{III} edge data, as the EXAFS oscillations from the underlying Ti K edge strongly interfere.

The data and fits for the pure material are shown in figure 4 and the fit parameters for all the data are summarized in tables 2 and 3. Amplitude data for $x = 0$, 0.1 and 0.4 samples are shown in figure 5. Both the data and the fits for the $x = 1.7$ data indicate that this sample is not close to a pure pyrochlore structure, and are not shown. Reported errors are from a Monte Carlo method, assuming that fit degrees of freedom can be obtained from Stern's rule [28]. R_{xrd} values are x-ray diffraction results from Lian *et al* [29].

The data and fit results for the pure $Ho_2Ti_2O_7$ material indicate a well-ordered material. The Ho edge data and fits for

Figure 5. (a) FT amplitudes of the $k^3\chi(k)$ EXAFS data from the Ho L_{III} edge and (b) FT of the $k^2\chi(k)$ of data from the Ti K edge for the $x = 0$, 0.1 and 0.4 samples, all at $T = 30$ K. Transform ranges are as in figure 4.

the $x = 0$, 0.1 and 0.4 samples are almost indistinguishable, although the σ^2 parameter for the first Ho–O(1) peak increases notably for the $x = 0.4$ data compared to the others, as does that for the Ho–Ti/Ho/La pairs. Interestingly, the Ti K-edge transforms are clearly different between the various samples, although this difference is not clearly indicated by the fit parameters. The σ^2 parameters for the first Ti–O(1) pairs do increase systematically, although not within the stated errors. The fit quality, however, gets noticeably worse with increasing x for the Ti edge data. Taken together, these data clearly indicate increasing disorder with x, especially for the $x = 0.4$ sample.

3.3. Quasi-elastic neutron scattering, TOF

Figure 6 shows the diffuse scattering observed at low temperature on a neutron time-of-flight spectrometer (DCS). The energy transfer was limited to ± 0.1 meV in the analysis. Again, one can see that the Bragg peaks for the $x = 1.7$ sample are at different positions than those of the samples with $x \leqslant 0.4$ because the structure is different.

The diffuse scattering observed in the data is indicative of short-ranged magnetic correlations very similar to those known for the spin ices [4, 30]. One can identify two maxima in the magnetic structure factor $S(Q)$ around $Q \sim 0.6$ Å^{-1} and $Q \sim 1.6$ Å^{-1}. At increasing x, the first maximum shifts slightly towards lower Q, which can be intuitively understood from the increased mean distance to nearest neighbours due to the additional voids. Within the energy resolution of the time-of-flight technique, the diffuse scattering shown in figure 6 appears elastic at temperatures below $T \sim 50$ K.

Table 2. $Ho_{2-x}La_xTi_2O_7$ fit results from Ho L_{III}-edge data at 30 K. Fit range is between 1.50 and 4.00 Å. The k^3-weighted data are transformed between 2.50 and 14.30 Å^{-1} and are Gaussian narrowed by 0.30 Å^{-1}. Multiple scattering was included in the fits, but the results for those peaks are not shown. Absolute errors are typically 0.005 Å in R and 10% in σ^2 for the nearest neighbours, and double for the further neighbours.

	$x = 0.0$				$x = 0.1$			$x = 0.4$		
	N	σ^2 (Å^2)	R (Å)	R_{xrd}	N	σ^2 (Å^2)	R (Å)	N	σ^2 (Å^2)	R (Å)
Ho–O(2)	2	0.0020(5)	2.189(5)	2.188	2	0.0028(4)	2.185(3)	2	0.0025(2)	2.187(2)
Ho–O(1)	6	0.0059(5)	2.471(4)	2.489	6	0.0056(2)	2.478(2)	6	0.0066(1)	2.480(1)
Ho–Ti	6	0.0039(6)	3.576(1)	3.572	6	0.0037(1)	3.580(2)	6	0.0047(1)	3.587(1)
Ho–Ho	6	0.0018	3.576	3.572	5.7	0.0017	3.580	4.8	0.0021	3.587
Ho–La	—	—	—	—	0.3	0.0018	3.580	1.2	0.0023	3.587
Ho–O(1)	12	0.009(1)	4.01(1)	4.072	12	0.008(1)	4.015(6)	12	0.0078(7)	4.044
ΔE_0		−7.0(9)				−7.3(5)			−7.5(3)	
S_0^2		1.03(6)				1.03			1.03	
R (%)		3.87				3.90			2.72	

Table 3. $Ho_{2-x}La_xTi_2O_7$ fit results from Ti K-edge data at 30 K. Fit range is between 1.40 and 4.60 Å. For most fits, the k^2-weighted data are transformed between 3.5 and 11.4 Å^{-1} and are Gaussian narrowed by 0.30 Å^{-1}. The overall scale factor S_0^2 is obtained from fits to the $x = 0$ data that extend to 16.0 Å^{-1}. These fits also required a separate ΔE_0 for the first scatter pair, Ti–O(1). Multiple scattering was included in the fits, but the results for those peaks are not shown. Absolute errors are typically 0.005 Å in R and 10% in σ^2 for the nearest neighbours, and double for the further neighbours.

	$x = 0.0$				$x = 0.1$			$x = 0.4$		
	N	σ^2 (Å^2)	R (Å)	R_{xrd}	N	σ^2 (Å^2)	R (Å)	N	σ^2 (Å^2)	R (Å)
Ti–O(1)	6	0.0023(3)	1.964(6)	1.954	6	0.0026(5)	1.96(1)	6	0.0033(9)	1.96(1)
Ti–Ti	6	0.0031(4)	3.550(7)	3.572	6	0.0021(6)	3.58(1)	6	0.0035(8)	3.63(1)
Ti–Ho	6	0.0020	3.550	3.572	5.7	0.0014	3.58	4.8	0.0022	3.63
Ti–La	—	—	—	—	0.3	0.0014	3.58	1.2	0.0023	3.63
Ti–O(1)	6	0.008(4)	3.71(1)	3.769	6	0.001(2)	3.76(3)	6	0.00(1)	3.83(2)
Ti–O(2)	6	0.008	4.13	4.16	6	0.001	4.19	6	0.00	4.245
Ti–O(1)	12	0.008	4.29	4.32	12	0.001	4.36	12	0.00	4.410
$\Delta E_{0,1}$		1(1)				2(3)			1(4)	
ΔE_0		2(1)				4(4)			−4(3)	
S_0^2		0.89				0.89			0.89	
R (%)		6.07				9.38			17.86	

An analysis of the time-averaged spatial spin correlations was carried out by means of a reverse Monte Carlo (RMC) technique. A cube of $6 \times 6 \times 6$ cubic unit cells was considered with magnetic moments situated at the 16d sites. An appropriate amount of them was replaced by non-magnetic voids whose positions were chosen randomly. Individual moments were constrained to be parallel to a local $\langle 111 \rangle$ axis, in line with the known spin anisotropy. Starting with an arbitrary spin configuration, a few spins were randomly chosen and flipped in one step of the simulation. A powder average of the cross section $d\sigma/d\Omega$ was then computed using

$$\frac{d\sigma}{d\Omega} = \text{const} \cdot F^2(Q) \cdot \sum_{m,n} \frac{\sin Q r_{m,n}}{Q r_{m,n}} \cdot \frac{\langle \boldsymbol{S}_m \cdot \boldsymbol{S}_n \rangle}{S(S+1)},$$

where m, n run through the cube, S denotes the moment on a site, $r_{m,n}$ is the distance between two sites, and $F(Q)$ is the magnetic form factor. The MC step was accepted if the fit to the measured intensity was improved, and repeated if not. The scale factor in the fit accounts for the fact that the measurement did not yield the scattering cross section in absolute units. Many individual MC runs were performed until convergence, and then linearly combined to produce the final best fit.

The fits to $d\sigma/d\Omega$ resulting from the reverse Monte Carlo simulation are also shown in the upper panel of figure 6, and the resulting time-averaged spin correlations for near-neighbour shells are shown in the lower panel. Even for nearest neighbours these correlations are very small, $\langle \boldsymbol{S}_m \cdot \boldsymbol{S}_n \rangle / S(S+1) \sim +0.07$ in the nearest-neighbour shell. In the first-neighbour shell the correlations are net ferromagnetic and in the next-neighbour shells net antiferromagnetic. Overall the correlations are short ranged (do not extend beyond $\sim$10 Å) with little effect of doping.

3.4. Quasi-elastic neutron scattering, BS and NSE

The data obtained with the high-resolution scattering instruments—neutron backscattering and spin echo—show that the diffuse scattering is dynamic at temperatures $T >$ 1 K. These two techniques are complimentary in that (i) backscattering measures neutron energy transfer $\hbar\omega$ while spin echo—as a Fourier technique—works in the time domain, and (ii) they cover somewhat different (but overlapping) ranges in energy transfer (or Fourier time).
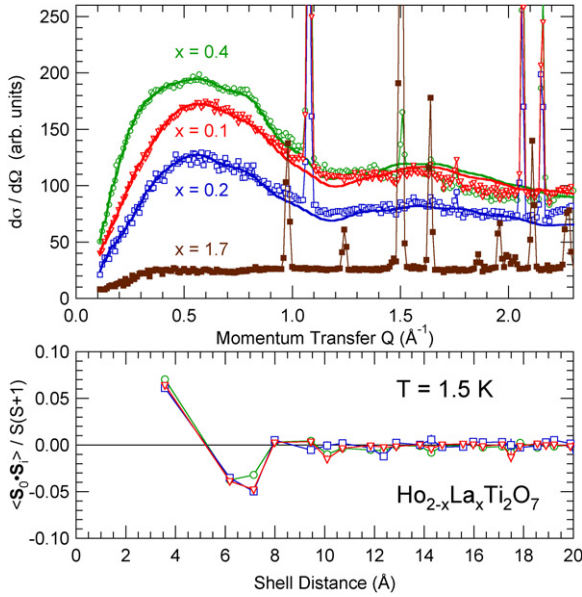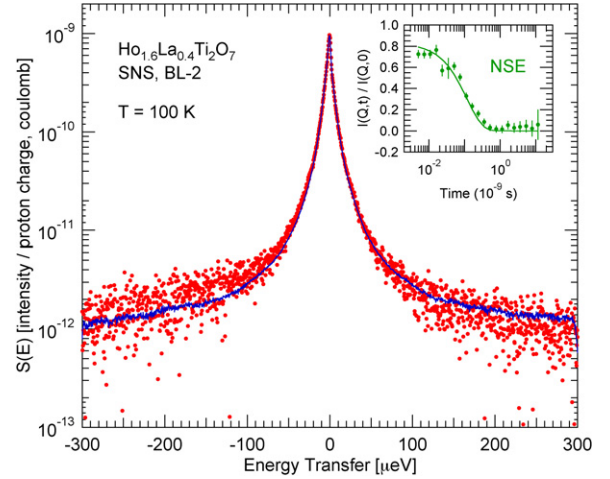
Figure 6. Diffuse magnetic scattering studied at DCS, corrected for vanadium and monitor intensities. The energy window was set to ± 0.1 meV. Intensity is highest at $x = 0.4$ because of the higher sample transmission. The diffuse $S(Q)$ has two maxima at 0.6 and 1.6 Å^{-1}, respectively. The upper panel also shows the fits, and the lower panel shows the resulting time-averaged spin correlations in the near-neighbour shells, from a reverse Monte Carlo simulation.

Figure 7. BS and NSE data and fits combined at $T = 100$ K for the $x = 0.4$ sample. For details, see text.

Figure 8. The spin correlation functions in the time domain. Shown are the data points from NSE with error bars arising from counting statistics and the fits of combined BS and NSE data as described in the text.

In the present study it is advantageous to combine these two techniques. As the data below show, in the spin echo time window (starting at 4×10^{-12} s) the information on the spin relaxation is incomplete, as there is already some correlation lost at the shortest time. The backscattering data, covering (via Fourier transform) a time range shifted to somewhat shorter times, covers the initial drop in the NSE signal but carries no information of the relaxation function at the longer times.
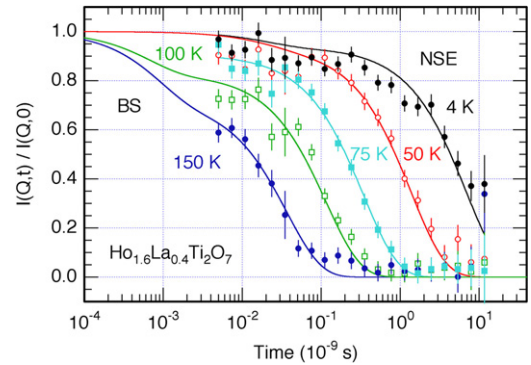
Figure 7 shows an example of the analysis of the combined BS and NSE data at $T = 100$ K. NSE and BS data were fitted simultaneously to the same scattering law, a double exponential in time, which reads

(NSE) $\qquad \dfrac{I(Q, t)}{I(Q, 0)} = A e^{-t/\tau_1} + (1 - A) e^{-t/\tau_2}$

(BS) $\qquad S(Q, \omega) = I_{\text{qel}} \left\{ A \dfrac{\Gamma_1}{(\Gamma_1)^2 + (\hbar\omega)^2} + (1 - A) \right.$

$\left. \times \dfrac{\Gamma_2}{(\Gamma_2)^2 + (\hbar\omega)^2} \right\} + I_{\text{el}} \delta(\omega)$

where $\Gamma_{1,2} = \hbar/\tau_{1,2}$, I_{qel} is the quasi-elastic intensity, the factor I_{el} allows for nuclear incoherent elastic intensity (which NSE does not see), and the detailed balance factor has been omitted, since $kT \gg \hbar\omega$. The NSE data is already corrected for instrumental resolution, while for the backscattering data the model function was convoluted with the instrumental resolution. The figure of merit optimized in these fits is the sum of the normalized χ^2 values of the two data sets. In the analysis of backscattering data it is often observed that an instrument background term strongly correlates with fit parameters of the line width. This problem has been mitigated here by the very

large dynamic range of the backscattering data, the very good signal/noise ratio, and by the correlation of the widths $\Gamma_{1,2}$ to the decay times in the NSE data.

It is intuitive to present the fit results in the time domain, which is done in figure 8. One can see that the combination of both BS and NSE data covers the full spin relaxation in the temperature range from 4 to 150 K while NSE alone only sees the slower of the two processes. The backscattering data also helped to confirm that the dynamics is independent of Q in the range from 0.3 to 2.0 Å^{-1}.

The relaxation times for the main relaxation process (index 2 above) compare very well with the results from pure spin ice [31]. The main difference to the pure spin ice is the apparent presence of a second relaxation process at a shorter timescale which has a smaller weight in the scattering (for the $x = 0.4$ sample, $A \sim 0.2$ at 100 K). This can be ascribed to 'defect-assisted' relaxation of Ho spins in the pyrochlore lattice. Even though the $x = 0.4$ sample has 10% contamination with a monoclinic phase, the DCS data (figure 6) showed that this phase does not contribute to the diffuse scattering. This can be seen in figure 6 by a comparison of the intensities around 0.6 Å^{-1}, noting that that the $x = 1.7$
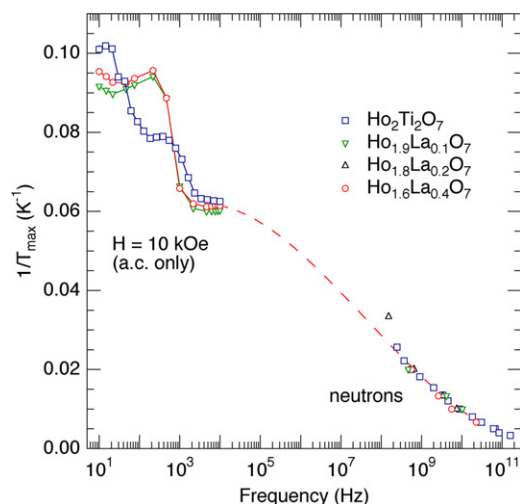
Figure 9. Combination of results from measurements of ac susceptibility (top left) and quasi-elastic neutron scattering (bottom right). For susceptibility, this graph shows the inverse of the temperatures at which the main maximum in the imaginary part occurs, as a function of the probing frequency, for the $x = 0, 0.1$ and 0.4 samples. For the neutron data, the inverse measurement temperature is plotted against the inverse of the main spin relaxation time, as fitted from either NSE or NSE and backscattering combined. Symbols used: $x = 0$ ($\square$), $x = 0.1$ ($\triangledown$), $x = 0.2$ ($\triangle$), $x = 0.4$ ($\circ$). The slope of the curve of the neutron data corresponds to an activation energy in the Arrhenius law of $\Delta \sim 290$ K.

sample is purely monoclinic while the $x = 0.4$ sample contains only 10% of monoclinic phase.

3.5. ac susceptibility

Bulk susceptibility measurements probe at much lower frequencies than neutron scattering, thus complementing the dynamic neutron experiments. Combined, these two types of probes span at least ten orders of magnitude in frequency (see figure 9). A gap from 10^4 to 10^8 remains open, but when the results are combined it appears that both techniques cover the same dynamical processes. Reports on ac susceptibility measurements on these and very similar systems have already been published [8, 14]. The imaginary part of the ac susceptibility shows a main peak at a frequency-dependent temperature. This is shown in the top left of figure 9. As discussed in the previous section, the neutron data also show one main relaxation mechanism whose frequency (inverse relaxation time) correlates with the measurement temperature, as shown in the bottom right of figure 9. The neutron data roughly follow an Arrhenius law, that is thermal activation, with an activation energy $\Delta \sim 290$ K. In the vicinity of freezing, the temperature dependence of the ac susceptibility data is more complicated, indicating the presence of several other processes, and is not fully understood at the present time.

4. Summary and conclusion

We have shown that the $(Ho–La)_2Ti_2O_7$ system adopts the pyrochlore structure up to a critical composition around $x = 0.3$. This is quite similar to the $Y_{2-x}La_xTi_2O_7$ series [25].

At higher La concentration the samples are bi-phasic with co-existing Ho-rich pyrochlore and La-rich monoclinic phases. Ho L_{III}-edge and Ti K-edge EXAFS data give consistent results, showing increasing local disorder with x. Neutron scattering experiments show that the frustrated spin–spin correlations in HTO are remarkably robust and not much affected by the chemical alteration which creates magnetic voids in the lattice. This holds for both the time-averaged correlations as well as the spin dynamics. To a small extent, although larger than in the $(Ho–Y)_2Ti_2O_7$ system [15], defect-assisted spin relaxation has been detected by high-resolution neutron spectroscopy.

References

[1] Bramwell S T *et al* 2001 *Science* **294** 1495
[2] Melko R G *et al* 2004 *J. Phys.: Condens. Matter* **16** R1277
[3] Ramirez A P *et al* 1999 *Nature* **399** 333
[4] Bramwell S T *et al* 2001 *Phys. Rev. Lett.* **87** 047205
[5] den Hertog B C *et al Phys. Rev. Lett.* **84** 3430
[6] Harris M J *et al* 1998 *J. Magn. Magn. Mater.* **177–181** 757
[7] Lago J *et al* 2007 *J. Phys.: Condens. Matter* **19** 326210
[8] Matsuhira K *et al* 2000 *J. Phys.: Condens. Matter* **12** L649
[9] Matsuhira K *et al* 2000 *J. Phys.: Condens. Matter* **13** L737
[10] Snyder J 2001 *Nature* **413** 48
[11] Snyder J 2002 *Phys. Rev.* B **66** 064432
[12] Snyder J 2004 *Phys. Rev.* B **70** 184431
[13] Ehlers G *et al* 2003 *J. Phys.: Condens. Matter* **15** L9
[14] Kajňaková M *et al* 2004 *J. Magn. Magn. Mater.* **272–276** e989
[15] Ehlers G *et al* 2006 *Phys. Rev.* B **73** 174429
[16] Subramanian M A *et al* 1983 *Prog. Solid State Chem.* **15** 55
[17] Schmalle H W *et al* 1993 *Acta Crystallogr.* B **49** 235
[18] Rodríguez-Carvajal J 1993 *Physica* B **192** 55
[19] Li G G *et al* 1995 *Phys. Rev.* B **52** 6332
[20] http://lise.lbl.gov/RSXAP/
[21] Ankudinov A L *et al* 1997 *Phys. Rev.* B **56** R1712
[22] Copley J R D *et al* 2003 *Chem. Phys.* **292** 477
[23] Mason T E *et al* 2006 *Physica* B **385/386** 955
[24] Ehlers G 2006 *J. Phys.: Condens. Matter* **18** R231
[25] Harvey E J *et al* 2006 *J. Mater. Chem.* **16** 4665
[26] Booth C H *et al* 2002 *Phys. Rev.* B **66** 140402(R)
[27] Han S W *et al* 2004 *Phys. Rev.* B **69** 024416
[28] Stern E A 1993 *Phys. Rev.* B **48** 9825
[29] Lian J *et al* 2003 *Phys. Rev.* B **68** 134107
[30] Mirebeau I *et al* 2004 *J. Phys.: Condens. Matter* **16** S653
[31] Ehlers G *et al* 2004 *J. Phys.: Condens. Matter* **16** S635